

# In Vivo Three-Dimensional Characterization of the Healthy Human Lamina Cribrosa With Adaptive Optics Spectral-Domain Optical Coherence Tomography

Zach Nadler,<sup>1</sup> Bo Wang,<sup>1,2</sup> Joel S. Schuman,<sup>1,2</sup> R. Daniel Ferguson,<sup>3</sup> Ankit Patel,<sup>3</sup> Daniel X. Hammer,<sup>4</sup> Richard A. Bilonick,<sup>1,5</sup> Hiroshi Ishikawa,<sup>1,2</sup> Larry Kagemann,<sup>1,2</sup> Ian A. Sigal,<sup>1,2</sup> and Gadi Wollstein<sup>1</sup>

<sup>1</sup>Department of Ophthalmology, University of Pittsburgh Medical Center Eye Center, Eye and Ear Institute, Ophthalmology and Visual Science Research Center, University of Pittsburgh School of Medicine, Pittsburgh, Pennsylvania, United States

<sup>2</sup>Department of Bioengineering, Swanson School of Engineering, University of Pittsburgh, Pittsburgh, Pennsylvania, United States

<sup>3</sup>Physical Sciences, Inc., Andover, Massachusetts, United States

<sup>4</sup>Center for Devices and Radiological Health, Food and Drug Administration, Silver Springs, Maryland, United States

<sup>5</sup>Department of Biostatistics, Graduate School of Public Health, University of Pittsburgh, Pittsburgh, Pennsylvania, United States

Correspondence: Joel S. Schuman, UPMC Eye Center, 203 Lothrop Street, Suite 816, Pittsburgh, PA 15213, USA; schumanjs@upmc.edu.

Submitted: July 7, 2014

Accepted: September 3, 2014

Citation: Nadler Z, Wang B, Schuman JS, et al. In vivo three-dimensional characterization of the healthy human lamina cribrosa with adaptive optics spectral-domain optical coherence tomography. *Invest Ophthalmol Vis Sci*. 2014;55:6459–6466. DOI:10.1167/iov.14-15177

**PURPOSE.** To characterize the in vivo three-dimensional (3D) lamina cribrosa (LC) microarchitecture of healthy eyes using adaptive optics spectral-domain optical coherence tomography (AO-SDOCT).

**METHODS.** A multimodal retinal imaging system with a light source centered at 1050 nm and AO confocal scanning laser ophthalmoscopy was used in this study. One randomly selected eye from 18 healthy subjects was scanned in a  $6^\circ \times 6^\circ$  window centered on the LC. Subjects also underwent scanning with Cirrus HD-OCT. Lamina cribrosa microarchitecture was semiautomatically segmented and quantified for connective tissue volume fraction (CTVF), beam thickness, pore diameter, pore area, and pore aspect ratio. The LC was assessed in central and peripheral regions of equal areas and quadrants and with depth. A linear mixed effects model weighted by the fraction of visible LC was used to compare LC structure between regions.

**RESULTS.** The nasal quadrant was excluded due to poor visualization. The central sector showed greater CTVF and thicker beams as compared to the periphery ( $P < 0.01$ ). Both superior and inferior quadrants showed greater CTVF, pore diameter, and pore mean area than the temporal quadrant ( $P < 0.05$ ). Depth analysis showed that the anterior and posterior aspects of the LC contained smaller pores with greater density and thinner beams as compared to the middle third ( $P < 0.05$ ). The anterior third also showed a greater CTVF than the middle third ( $P < 0.05$ ).

**CONCLUSIONS.** In vivo analysis of healthy eyes using AO-SDOCT showed significant, albeit small, regional variation in LC microarchitecture by quadrant, radially, and with depth, which should be considered in further studies of the LC.

**Keywords:** in vivo, OCT, structure

**G**laucoma is characterized by the progressive neurodegenerative loss of retinal ganglion cells and associated loss of visual function in characteristic patterns and locations. The lamina cribrosa (LC) is a collagenous meshwork located within the optic nerve head (ONH) and has been widely implicated as a key player in the pathogenesis of glaucoma.<sup>1</sup> The mechanical theory of glaucoma surmises that damage to the retinal ganglion cell axons associated with disease is due to an altered biomechanical environment within the LC.<sup>2</sup> Such an altered biomechanical environment could be from an elevated intraocular pressure (IOP) or a susceptible LC microarchitecture.<sup>3,4</sup> Hence, numerous studies have investigated the relationships between various LC microarchitecture measurements ex vivo and known regional risk of glaucomatous neuropathy. These studies reported that the regions at greater risk of glaucoma have decreased connective tissue toward the

peripheral LC and increased pore area in the superior and inferior quadrants with respect to the temporal and nasal quadrants.<sup>5–8</sup>

Efforts to document the in vivo relationship between detailed LC microarchitecture and disease face the challenges of visualizing a structure buried within the ONH and often obscured by more anterior reflective structures. Fundus photography and confocal scanning laser ophthalmoscopy (CSLO) studies have been used to measure pore size and shape in living human eyes and examine their relationship with disease.<sup>9,10</sup> Recently, adaptive optics has augmented scanning laser ophthalmoscopy studies to quantify detailed microstructure in primates and humans by improving transverse image resolution.<sup>11–14</sup> The information generated by these methods is either predominantly reflecting the anterior LC only (CSLO) or the light projection from the entire LC with overlay of many

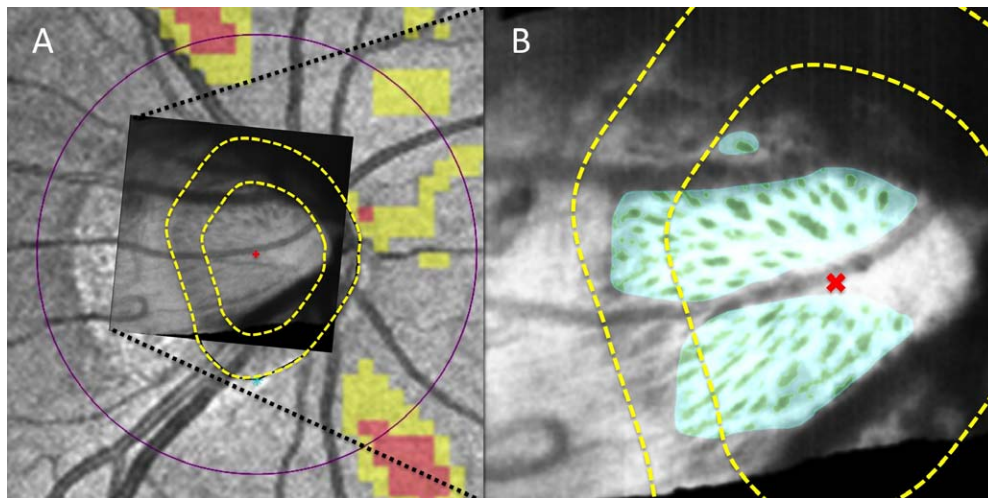


**FIGURE 1.** Overlay of AO-SDOCT on face average intensity projection on Cirrus OCT image (A) with disc delineation and disc center from Cirrus HD-OCT output allowing the segmentation into center and periphery regions (B).

pores and beams along the full depth of the LC (photography). Moreover, all of these studies are limited by poor axial resolution as well as information on depth.

Spectral-domain optical coherence tomography (SDOCT) with its high acquisition rate and improved penetration depth, when using enhanced depth imaging (EDI), allows the acquisition of three-dimensional (3D) images of the LC.<sup>15-19</sup> Manual delineation of the anterior LC surface, in combination with innovative methods for image contrast enhancement in the posterior LC, has enabled the quantification of LC depth and volume in studies of the relationship between overall LC shape with disease.<sup>19-22</sup> Apparent anterior defects and full-thickness deformations have also shown correspondence with disease.<sup>23-25</sup> Recently, pore and beam structure has been probed in healthy and glaucomatous eyes and revealed some discord in the ratio of pore to beam width between the groups.<sup>26</sup> These microarchitecture changes were assessed using an automated segmentation method that was both sensitive to detect pore structure<sup>27</sup> and repeatable.<sup>28</sup> However, these changes were assessed globally, and a detailed evaluation of microarchitecture on a regional basis has been accomplished only in ex vivo studies of the LC.<sup>6,8</sup> The emergence of powerful in vivo imaging devices and image processing tools allows detailed visualization and analysis of the 3D configuration of the LC, though a thorough description of the microarchitecture of the healthy LC is required to enable future investigation in the presence of disease. The purpose of this study was to characterize the in vivo 3D structure of healthy LC globally and regionally in both coronal and sagittal dimensions.

## METHODS

### Subjects

Subjects were enrolled at the University of Pittsburgh Medical Center Eye Center. All subjects were recruited in accordance with the tenets of the Declaration of Helsinki and the Health Insurance Portability and Accountability Act. This study was approved by the institutional review board of the University of Pittsburgh, and all subjects provided written informed consent prior to participation. All subjects underwent comprehensive ophthalmic examination, including optic nerve assessment, measurement of IOP, Swedish interactive thresholding algorithm 24-2 standard perimetry, and OCT imaging. Only healthy

eyes showing normal appearance of the ONH and retinal nerve fiber layer, with full visual fields and without any previous history of ocular diseases or glaucoma, were included in the study. Although there were no specific exclusion criteria for myopia or myopic discs, the maximum refractive error was  $-4.25$  diopters (D).

### Image Acquisition and Analysis

Each subject was scanned with the Cirrus HD-OCT (Zeiss, Dublin, CA, USA) and a multimodal retinal imaging system with adaptive optics, which included an adaptive optics (AO)-SDOCT imaging channel, as well as AO-CSLO (Physical Sciences, Inc., Andover, MA, USA). The multimodal retinal imaging device has been previously described in detail.<sup>29</sup> Briefly, the light source for the AO-SDOCT was a superluminescent diode (SLED) centered at 1050 nm, which allowed deeper tissue penetration than common commercial scanners that typically use a shorter  $\sim 850$ -nm light source. Adaptive optics correction permitted transverse and axial resolutions of 5 and 4.5  $\mu\text{m}$ , respectively. Scans with both devices were centered on the LC. The AO-SDOCT acquired in EDI a  $6^\circ \times 6^\circ$  data volume ( $1.5 \times 1.5$  mm) with 512 samplings per A-scan, 1024 A-scans per B-scan, and 200 B-scans per volume at a scanning rate of 28 kHz, for a scan time of  $\sim 7$  seconds. Cirrus HD-OCT scanning protocol was the ONH  $200 \times 200$  cube scan ( $6 \times 6$  mm). Prior to scanning, pupils were dilated with tropicamide. One eye of each subject was randomly selected for analysis.

Adaptive optics-SDOCT scans were processed<sup>30</sup> and microarchitecture was semiautomatically delineated using a previously described method<sup>27</sup> of smoothing and automated local thresholding, which has demonstrated high repeatability.<sup>28</sup> Scan quality was subjectively evaluated considering the following factors: movement artifacts uncorrected in automated registration sequence, contrast between beams and pores, automated microarchitecture segmentation quality, and the area of visible LC. Poor-quality scans were removed prior to the statistical analysis.

Each AO-SDOCT scan was registered to Cirrus HD-OCT scans of the corresponding eye using average intensity projections of the AO-SDOCT C-mode volume stack (Fig. 1). The disc delineation automatically output from Cirrus HD-OCT was used as the exterior margin for determining the extent of

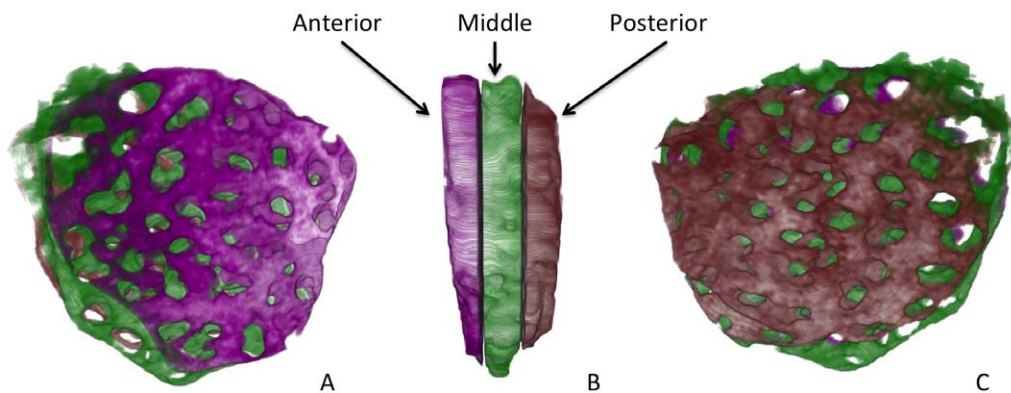


FIGURE 2. Delineation with depth permits 3D visualization from the anterior (A), side (B), and posterior (C) surfaces, which are divided into three regions for depth analysis.

visible lamina in each quadrant. This landmark was also used as the peripheral LC boundary to divide each LC into central and peripheral regions of equal areas. The disc center taken from the Cirrus HD-OCT scans was also used to divide the AO-SDOCT volume into superior, temporal, inferior, and nasal quadrants. In addition, the visible LC was divided equally into three thirds: anterior, middle, and posterior (Fig. 2). The thickness of the visible thirds varied depending on the thickness of the visible LC. The anterior surface of the LC often showed characteristic “U” or “W” shapes, which have been previously described,<sup>19,20</sup> with some segments of the tissue obscured due to shadowing from other more anterior structures. Therefore, parameterization by depth was performed both with respect to the first C-mode slice where the LC was visible (primary analysis) and relative to the image-processed flattened anterior LC surface (secondary analysis; Fig. 3).

Three-dimensional parameters considered in the analysis included beam thickness, pore diameter, and connective tissue volume fraction (CTVF) computed as the ratio of voxels marked as beams to the total volume of analyzed LC. Beam thickness and pore diameter were calculated using BoneJ (bonej.org [in the public domain]), which assigns thickness values to each voxel by the diameter of the largest enclosing sphere.<sup>31</sup> Analysis of C-mode slices provided a size distribution for cross-sectional pore areas as well as pore mean area, pore aspect ratio, and pore density (Fig. 4).

**Statistical Analysis**

Statistical analysis was conducted using the R Language and Environment for Statistical Computing software (version 2.15.1).<sup>32</sup> Tissue visibility was determined by the ratio of observable LC, using C-mode maximum intensity projections from the AO-SDOCT, to the spatially registered Cirrus HD-OCT disc boundary. A linear mixed effects model was used to evaluate the effect of region, depth, subject, and age on the

measured parameters. In order to allow comparison between regions, weighting was applied based on the tissue visibility. Statistical significance was set at  $P < 0.05$ .

**RESULTS**

The study population included 32 eyes, and after exclusion of poor-quality images, 18 eyes from 18 subjects qualified for analysis (12 women, 6 men; 11 OD, 7 OS) with a mean age of  $32.9 \pm 12.9$  years. Subjective evaluation of the C-mode projections of AO-SDOCT LC showed good correspondence with Cirrus en face images.

**Lamina Visibility**

Overall, 21% of the total LC was visible among all analyzed eyes. The central region of the lamina was substantially more visible than the peripheral regions (Table 1). The temporal aspect of the LC had the greatest visibility (56.0%) while the nasal region had the lowest visibility (6.9%). Because of the poor visibility of the nasal quadrant, it was excluded from further analysis. Visibility varied substantially between subjects, and there was no significant correlation of visibility between quadrants ( $r^2$  range, 0.01–0.04;  $P > 0.05$  for all).

**Pore Size Distribution**

Distributions of cross-sectional pore area plotted for all the pores in each subject revealed some variability in the distribution of pore sizes between subjects (Fig. 5). An overall trend toward a positively skewed distribution with greater numbers of small pores was observed.

**Central and Peripheral LC**

Pore diameter and beam thickness were statistically significantly smaller in the periphery compared to central lamina

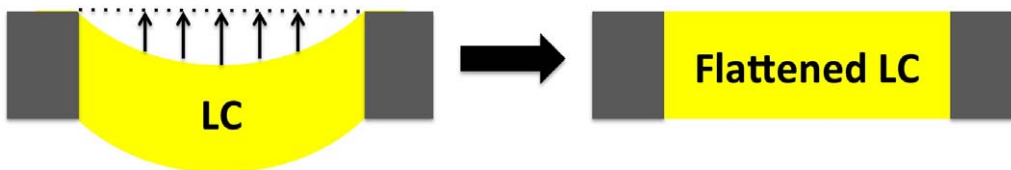
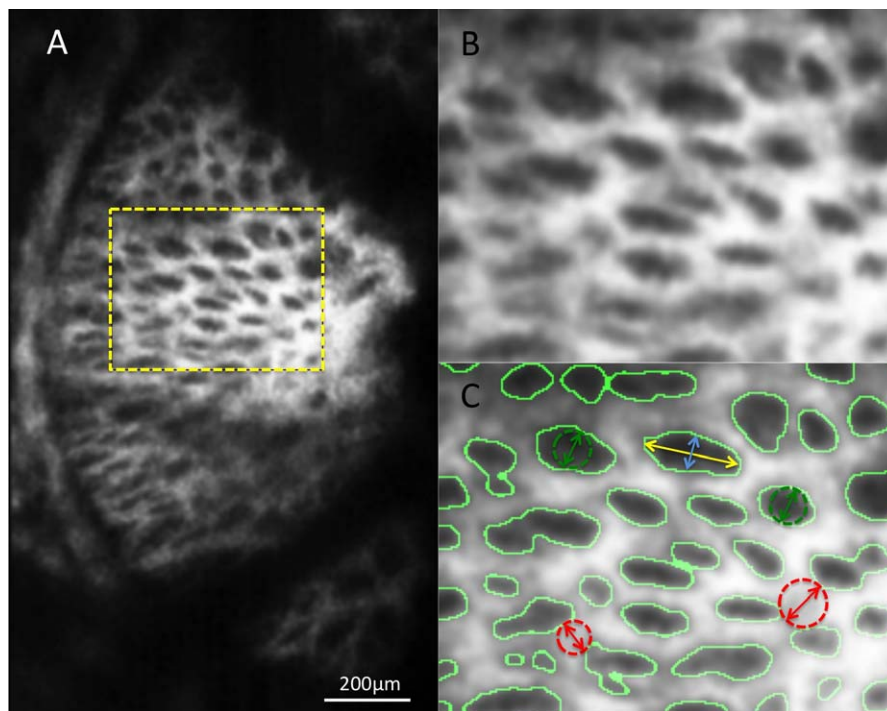


FIGURE 3. Schematic of flattening procedure for secondary depth analysis of LC.



**FIGURE 4.** Quantification of LC pores and beam structure performed in cross section (A) and magnified (B, C). Pores were segmented using automated technique, with the boundary between beam and pore shown with the *solid green line* (C). Parameters such as pore mean area and aspect ratio (ratio of *long yellow arrow* to *short blue arrow*) were calculated as the average of all pores observed. Beam thickness (*green arrow* and *dotted lines*) and pore diameter were calculated voxel-wise using method of expanding spheres and then averaged (C).

(Table 2). However, pore mean area was not statistically different between these regions, leading to lower CTVF and substantially higher pore density in the periphery.

**Quadrant Analysis**

Quadrant comparison showed no significant difference between superior and inferior quadrants for any of the parameters (Table 3). The superior quadrant had larger pore diameter with smaller aspect ratio and more connective tissue with respect to the temporal quadrant. The inferior quadrant had smaller mean pore area than the temporal quadrant. For the cohort, mean pore area was larger in the inferior than in the temporal quadrant, but within eyes the trend reversed, with larger pores in the temporal region ( $P < 0.05$ ).

**Depth Analysis**

Analysis with depth showed similar microarchitecture in the anterior and posterior thirds of the LC (Table 4). However, both the anterior and posterior aspects of the LC had an increased density of smaller pores and beams as compared to

the middle third, with a greater CTVF in the anterior third with respect to the middle.

In the secondary analysis, we flattened the anterior surface of the lamina to account for the various patterns of anterior surface. After flattening, the differences were a significantly larger CTVF in the anterior third compared with the middle and reduced beam and pore thickness in the posterior with respect to the middle.

**Parameter Associations**

There was a highly significant association between LC parameters, except for pore density, and CTVF (Table 5). In general, thicker beams were associated with larger pores, at a lower pores aspect ratio and density, and an overall increase in CTVF.

**DISCUSSION**

This study was designed to characterize the in vivo 3D microarchitecture of the healthy LC. Adaptive optics-SDOCT with a 1050-nm centered light source was used for optimal visualization of LC microarchitecture. The use of a semi-automated segmentation technique permitted detailed 3D quantification of the lamina.<sup>27,28</sup> We detected small but significant variation in microarchitecture when analyzed radially, by quadrant, and with depth.

The quantification and regional comparison of microarchitecture in humans have been performed previously in histology and in vivo studies using disc photography and CSLO.<sup>5-9,12,33</sup> The intersubject variation in pore size and the positively skewed distribution we report have been shown in other cohorts ex vivo.<sup>6</sup> Our observation of decreased CTVF in the peripheral LC is also consistent with the literature.<sup>6</sup> The precise values for CTVF in our study are similar to or slightly

**TABLE 1.** Average Lamina Cribrosa Visible Area Fraction Computed With Respect to the Cirrus Disc for Each Region

Region	Visualized Area, %		Total
	Central	Peripheral	
Overall	32.8	10.4	21.1
Superior	32.5	8.3	18.6
Temporal	78.1	35.7	56.0
Inferior	20.7	5.1	11.8
Nasal	14.1	0.0	6.9

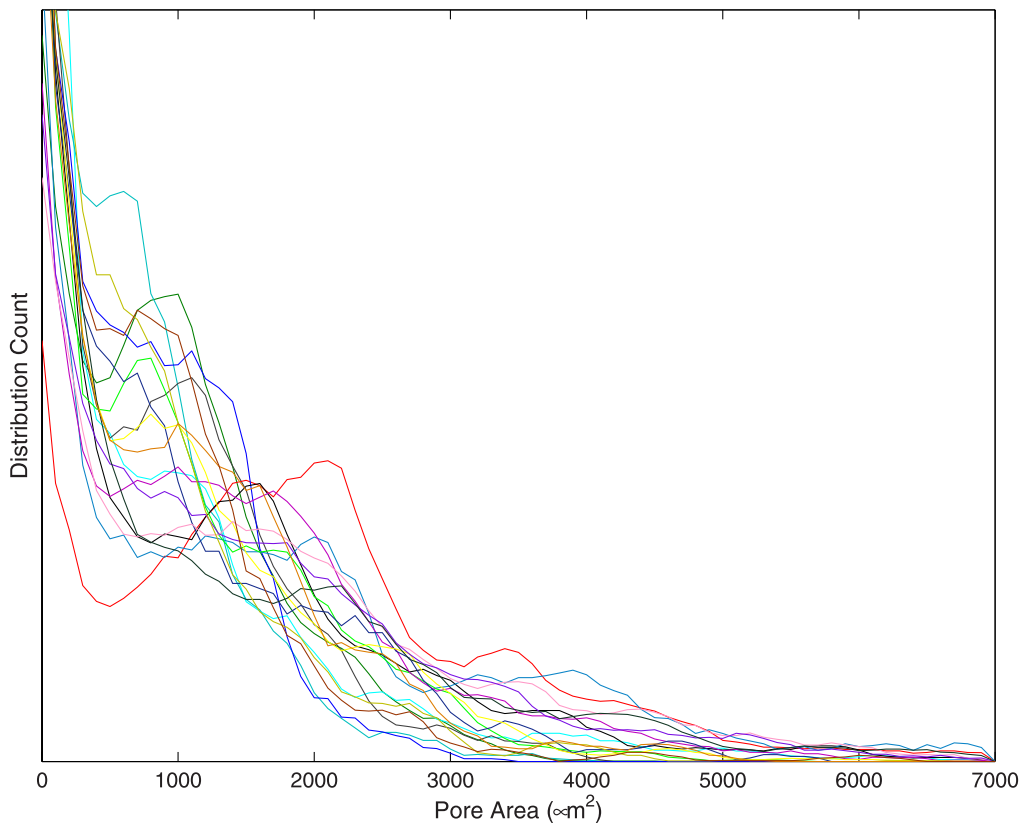


FIGURE 5. Pore size distribution for all subjects showing the intersubject variability in distribution shape but an overall trend toward a greater number of smaller pores.

TABLE 2. Central and Peripheral Lamina Cribrosa Microarchitecture Measurements; Values Reported as Mean (Standard Deviation) or Difference (% Difference Relative to the Central Value)

	Overall	Central	Peripheral	Central-Peripheral Difference*	P*
Beam thickness, μm	38.1 (1.4)	38.8 (1.8)	35.1 (1.0)	-2.2 (-5.2%)	<0.01
Pore diameter, μm	27.9 (1.6)	28.5 (1.9)	26.5 (1.1)	-0.6 (-2.1%)	0.03
Pore mean area, μm <sup>2</sup>	1302 (173)	1340 (207)	1205 (144)	-21 (-1.6%)	0.74
Pore mean AR	2.09 (0.06)	2.09 (0.10)	2.13 (0.05)	0.08 (3.8%)	0.18
Pore density, pores/mm <sup>3</sup>	2311 (280)	2208 (329)	2662 (253)	338 (15.3%)	0.02
CTVF, %	69.6 (1.2)	69.9 (1.5)	68.6 (1.0)	-1.8 (-2.6%)	<0.01

AR, aspect ratio.

\* Differences and P values are for the comparison between central and peripheral measurements using a linear mixed effects model.

TABLE 3. Lamina Cribrosa Measurement Comparison Between Quadrants; Values Reported as Mean (Standard Deviation)

	Sup	Temp	Inf	P*		
				Sup vs. Inf	Sup vs. Temp	Inf vs. Temp
Beam thickness, μm	38.9 (2.0)	37.2 (1.9)	38.2 (1.1)	0.17	0.08	0.51
Pore diameter, μm	29.3 (1.6)	27.1 (2.4)	28.8 (1.6)	0.80	<0.01	0.74
Pore mean area, μm <sup>2</sup>	1346 (163)	1286 (316)	1319 (129)	0.99	0.29	0.01
Pore mean AR	2.04 (0.06)	2.12 (0.13)	2.13 (0.10)	0.31	0.04	0.39
Pore density, pores/mm <sup>3</sup>	2205 (288)	2424 (477)	2202 (189)	0.87	0.65	0.08
CTVF, %	70.0 (1.5)	69.1 (1.9)	70.0 (1.4)	0.60	0.03	0.09

Sup, superior; Temp, temporal; Inf, inferior.

\* P value for the comparison between quadrant measurements using a linear mixed effects model.

TABLE 4. Parameter Means (Standard Deviation) as a Function of Lamina Cribrosa Depth

	Anterior	Middle	Posterior	P*		
				Ant vs. Post	Ant vs. Mid	Post vs. Mid
Beam thickness, $\mu\text{m}$	37.4 (1.7)	38.9 (1.4)	37.0 (1.4)	0.66	<0.01	<0.01
Pore diameter, $\mu\text{m}$	27.2 (1.5)	28.5 (1.7)	27.9 (1.7)	0.23	0.03	0.32
Pore mean area, $\mu\text{m}^2$	1202 (151)	1377 (191)	1285 (207)	0.19	<0.01	0.03
Pore mean AR	2.10 (0.05)	2.09 (0.07)	2.09 (0.08)	0.86	0.81	0.98
Pore density, pores/ $\text{mm}^3$	2407 (283)	2206 (280)	2440 (350)	0.74	<0.01	0.02
CTVF, %	70.5 (1.4)	69.4 (1.3)	69.1 (1.2)	0.06	0.04	0.49

Ant, anterior; Mid, middle; Post, posterior.

\* P value for the comparison between various depth measurements using a linear mixed effects model.

larger than those reported in another study (0.49–0.60),<sup>6</sup> which is probably due to the acquisition of the measurements in vivo compared to ex vivo in the other study. However, the range of CTVF detected in our population and within individual eyes was smaller.<sup>6,34</sup> While we observed significantly reduced CTVF and beam thickness in the periphery, the differences are small and unlikely to suggest biomechanical significance. The observation of narrower pores in the periphery conflicted with past results, and could be due to the limited visibility of the lamina with OCT when compared to the methods used in the previous studies.<sup>6,8</sup> The full LC periphery is unavailable to most OCT images; and if the largest pores are found at the LC edge, then our measurement of pore size in the periphery may be an underestimate. The increase in pore density may suggest that despite the smaller pore diameter, a comparable flux of axons traverses the peripheral LC.

The larger pores found in the superior quadrant could reflect the increased number of retinal ganglion cell axons traversing this section of the LC following their arcuate retinal projections.<sup>5</sup> Conversely, the relationship of pore area between inferior and temporal quadrants was somewhat enigmatic. Overall, the inferior had larger pores than the temporal quadrant, but within eyes, the larger pores appeared in the temporal quadrant. This may be a result of diminished visualization; in the inferior quadrant, a relatively small fraction of the tissue was available for analysis (Table 1). The inferior quadrant microarchitecture parallels the superior structure for many parameter values, but the visibility of this region is only approximately two-thirds the amount of tissue visible in the superior quadrant, which was accounted for in our statistical model. The effect of visualization is made apparent by considering the CTVF relationships between quadrants. The inferior and superior quadrants have nearly identical averages and standard deviations, but only the superior exhibits a significant difference from the temporal quadrant. The modest increase in visible tissue available in the superior quadrant allows for the identification of regional differences. Another consideration when analyzing differences between quadrants is the intersubject variability in major retinal nerve fiber layer (RNFL) bundle location. A temporally located major bundle may project more axons into the temporal LC quadrant, and a

detailed comparison between RNFL thickness and LC microarchitecture would better probe this relationship.

Pore shape has been implicated as a potential cofactor in relation to glaucoma, where a more elongated shape is thought to be associated with worsening disease.<sup>9,35</sup> Through pore aspect ratio we observed a more circularly shaped pore in the superior quadrant than in the temporal quadrant. This may reflect the surrounding beams having a horizontal orientation associated with the ridge previously reported spanning the horizontal meridian.<sup>21</sup>

The principal advantage of OCT in relation to other modes of in vivo imaging is the high axial resolution. The complexity of microarchitecture as a function of depth can be visualized in the intricate fenestrations and bifurcations of pores as they traverse the LC.<sup>5</sup> This also allowed the quantification of structure at different depths of the LC. Recent OCT studies have reported anterior defects in the LC to be correlated with RNFL defects and deficits in the visual field.<sup>23–25</sup> If tissue remodeling in the LC is preferentially targeting a specific depth of the LC, then it should be evident in microarchitecture, and probing the structure in a healthy cohort elucidates the normal physiologic differences between regions. We observed significant differences in structure as we moved posteriorly from the anterior surface of the LC. The anterior LC is densely populated with smaller pores and beams, which then congregate and combine into fewer larger pores, giving way to larger beams in the middle LC. The transition from middle to posterior LC reverts back to smaller, densely spaced pores. This may signify that the anterior and posterior surfaces of the LC are less ordered regions with a number smaller axonal bundles, which are then merged into thicker tunnels for the internal traverse across the LC. These spatial differences along the depth of the LC might also play a role in the localized sensitivity to glaucomatous damage.

The high degree of interrelation between various parameters indicates that the microarchitecture has consistent relationships between pores and beams of certain sizes. The association of larger pores with thicker beams suggests that larger pores may require greater biomechanical support from surrounding connective tissue. It's not surprising that pore density is inversely related to beam thickness and pore

TABLE 5. Associations Between LC Parameters Presented as Slopes (P Value) Determined Using Linear Mixed Effects Model

	Pore Diameter	Pore Mean Area	Pore Mean AR	Pore Density	CTVF
Beam thickness	0.66 (<0.01)	1.7E-3 (<0.01)	-1.4 (<0.01)	-4.3E-4 (<0.01)	8.4 (<0.01)
Pore diameter		3.5E-3 (<0.01)	-1.4 (<0.01)	-4.5E-4 (<0.01)	-15 (<0.01)
Pore mean area			3.1E-2 (<0.01)	-7.5E-2 (<0.01)	-6.0E-3 (<0.01)
Pore mean AR				1.5E-5 (0.02)	-1.4 (<0.01)
Pore density					7.7E-2 (0.38)

diameter; tightly packed pores interrupt beam structure and restrict overall pore area.

The foremost limitation of in vivo LC imaging is visualization and quantification of the full structure. Anterior vasculature, along with neural and prelaminar tissue, inhibits the ability to image the entire structure, and intuitively these difficulties may preferentially affect healthy eyes, where more neural tissue exists and the major blood vessels are more centrally located.<sup>36</sup> Techniques for contrast enhancement in shadowed regions such as adaptive compensation<sup>22</sup> may prove useful in future studies, but currently there is not an adequate means of resolving the fine structure of the microarchitecture in regions of low signal. This inevitable limitation of the OCT technology was partially mitigated in this study by using longer-wavelength light than that used in most conventional commercial devices to allow better tissue penetration. Furthermore, we analyzed the LC only where sufficient visibility and quality were achieved. When assessing the differences in microarchitecture between regions, weighting was applied based on the fraction of observable tissue compared to the Cirrus HD-OCT disc. Our underlying assumption was that regions with greater visibility provided more reliable structural means than those where only a small fragment of tissue was available for measurement. As a consequence, the model considered eyes with significant visibility in multiple regions more heavily when testing regional differences. This may also explain the curious result when pore area was compared between the inferior and temporal quadrants. The extent of the Cirrus HD-OCT disc is expected to be smaller than the full LC area<sup>36</sup>; thus our measurements may not extend to the full periphery.

In vivo determination of the posterior boundary of the LC has been a point of contention. In this study, the posterior boundary of the LC was marked as the last C-mode slice where there was apparent contrast in pore and beam structure. While previous studies have suggested that OCT is capable of capturing the entire LC thickness,<sup>18</sup> we cannot be certain that our visible posterior boundary corresponds with the true anatomical posterior LC boundary. It should be noted that we used a long-wavelength light source in our device, ensuring favorable tissue penetration as compared to studies where commercially available devices were used. Further investigation is warranted.

Cirrus HD-OCT disc delineations were used because they provided a standard accepted marking of the disc boundary, which used a scan encompassing the entire region of the ONH. By contrast, AO-SDOCT scans sometimes did not capture the full lateral extent of the disc, particularly in the nasal direction (Fig. 1). Additionally, AO narrows the depth of focus, hindering identification of the scleral canal opening—the standard feature for marking the disc boundary.

In conclusion, we report regional differences in microarchitecture in healthy LC as obtained in vivo using 3D AO-OCT scans. Observed structural variation should prove useful in further evaluation of the role of LC microarchitecture in glaucoma.

### Acknowledgments

Supported in part by National Institutes of Health Contracts R01-EY013178, R01-EY023966, R44-EY018986, P30-EY008098, and T32-EY017271 (Bethesda, MD, USA); Eye and Ear Foundation (Pittsburgh, PA, USA); and Research to Prevent Blindness (New York, NY, USA).

The mention of commercial products, their sources, or their use in connection with material reported herein is not to be construed as either an actual or implied endorsement of such products by the US Department of Health and Human Services.

Disclosure: **Z. Nadler**, None; **B. Wang**, None; **J.S. Schuman**, P; **R.D. Ferguson**, Physical Science, Inc. (E); **A. Patel**, Physical Science, Inc. (E); **D.X. Hammer**, Physical Science, Inc. (C); **R.A. Bilonick**, None; **H. Ishikawa**, None; **L. Kagemann**, None; **I.A. Sigal**, None; **G. Wollstein**, None

### References

1. Quigley HA. Glaucoma: macrocosm to microcosm the Friedenwald lecture. *Invest Ophthalmol Vis Sci.* 2005;46:2662-2670.
2. Fechtner RD, Weinreb RN. Mechanisms of optic nerve damage in primary open angle glaucoma. *Surv Ophthalmol.* 1994;39:23-42.
3. Burgoyne CF, Downs JC, Bellezza AJ, Suh J-KF, Hart RT. The optic nerve head as a biomechanical structure: a new paradigm for understanding the role of IOP-related stress and strain in the pathophysiology of glaucomatous optic nerve head damage. *Prog Retin Eye Res.* 2005;24:39-73.
4. Sigal IA, Ethier CR. Biomechanics of the optic nerve head. *Exp Eye Res.* 2009;88:799-807.
5. Quigley HA, Addicks EM. Regional differences in the structure of the lamina cribrosa and their relation to glaucomatous optic nerve damage. *Arch Ophthalmol.* 1981;99:137.
6. Dandona L, Quigley HA, Brown AE, Enger C. Quantitative regional structure of the normal human lamina cribrosa. A racial comparison. *Arch Ophthalmol.* 1990;108:393-398.
7. Jonas JB, Mardin CY, Schlötzer-Schrehardt U, Naumann GO. Morphometry of the human lamina cribrosa surface. *Invest Ophthalmol Vis Sci.* 1991;32:401-405.
8. Brown DJ, Morishige N, Neekhra A, Minckler DS, Jester JV. Application of second harmonic imaging microscopy to assess structural changes in optic nerve head structure ex vivo. *J Biomed Opt.* 2007;12:024029.
9. Tezel G, Trinkaus K, Wax MB. Alterations in the morphology of lamina cribrosa pores in glaucomatous eyes. *Br J Ophthalmol.* 2004;88:251-256.
10. Fontana L, Bhandari A, Fitzke FW, Hitchings RA. In vivo morphometry of the lamina cribrosa and its relation to visual field loss in glaucoma. *Curr Eye Res.* 1998;17:363-369.
11. Vilupuru AS, Rangaswamy NV, Frishman LJ, Smith EL III, Harwerth RS, Roorda A. Adaptive optics scanning laser ophthalmoscopy for in vivo imaging of lamina cribrosa. *J Opt Soc Am A Opt Image Sci Vis.* 2007;24:1417-1425.
12. Ivers KM, Li C, Patel N, et al. Reproducibility of measuring lamina cribrosa pore geometry in human and nonhuman primates with in vivo adaptive optics imaging. *Invest Ophthalmol Vis Sci.* 2011;52:5473-5480.
13. Akagi T, Hangai M, Takayama K, Nonaka A, Ooto S, Yoshimura N. In vivo imaging of lamina cribrosa pores by adaptive optics scanning laser ophthalmoscopy. *Invest Ophthalmol Vis Sci.* 2012;53:4111-4119.
14. Sredar N, Ivers KM, Queener HM, Zouridakis G, Porter J. 3D modeling to characterize lamina cribrosa surface and pore geometries using in vivo images from normal and glaucomatous eyes. *Biomed Opt Express.* 2013;4:1153-1165.
15. Kagemann L, Ishikawa H, Wollstein G, et al. Ultrahigh-resolution spectral domain optical coherence tomography imaging of the lamina cribrosa. *Ophthalmic Surg Lasers Imaging.* 2008;39(4 suppl):S126-S131.
16. Inoue R, Hangai M, Kotera Y, et al. Three-dimensional high-speed optical coherence tomography imaging of lamina cribrosa in glaucoma. *Ophthalmology.* 2009;116:214-222.
17. Park SC, De Moraes CGV, Teng CC, Tello C, Liebmann JM, Ritch R. Enhanced depth imaging optical coherence tomography of deep optic nerve complex structures in glaucoma. *Ophthalmology.* 2011;119:3-9.

18. Park H-YL, Jeon SH, Park CK. Enhanced depth imaging detects lamina cribrosa thickness differences in normal tension glaucoma and primary open-angle glaucoma. *Ophthalmology*. 2011;119:10-20.
19. Lee EJ, Kim T-W, Weinreb RN, et al. Three-dimensional evaluation of the lamina cribrosa using spectral-domain optical coherence tomography in glaucoma. *Invest Ophthalmol Vis Sci*. 2012;53:198-204.
20. Lee EJ, Kim T-W, Weinreb RN. Improved reproducibility in measuring the lamina thickness on enhanced depth imaging SD-OCT images using maximum intensity projection. *Invest Ophthalmol Vis Sci*. 2012;53:7576-7582.
21. Park SC, Kiumehr S, Teng CC, Tello C, Liebmann JM, Ritch R. Horizontal central ridge of the lamina cribrosa and regional differences in lamina insertion in healthy subjects. *Invest Ophthalmol Vis Sci*. 2012;53:1610-1616.
22. Mari JM, Strouthidis NG, Park SC, Girard MJA. Enhancement of lamina cribrosa visibility in optical coherence tomography images using adaptive compensation. *Invest Ophthalmol Vis Sci*. 2013;54:2238-2247.
23. Kiumehr S, Park SC, Syril D, et al. In vivo evaluation of focal lamina cribrosa defects in glaucoma. *Arch Ophthalmol*. 2012;130:552-559.
24. Park SC, Hsu AT, Su D, et al. Factors associated with focal lamina cribrosa defects in glaucoma. *Invest Ophthalmol Vis Sci*. 2013;54:8401-8407.
25. Tatham AJ, Miki A, Weinreb RN, Zangwill LM, Medeiros FA. Defects of the lamina cribrosa in eyes with localized retinal nerve fiber layer loss. *Ophthalmology*. 2014;121:110-118.
26. Wang B, Nevins JE, Nadler Z, et al. In vivo lamina cribrosa micro-architecture in healthy and glaucomatous eyes as assessed by optical coherence tomography. *Invest Ophthalmol Vis Sci*. 2013;54:8270-8274.
27. Nadler Z, Wang B, Wollstein G, et al. Automated lamina cribrosa microstructural segmentation in optical coherence tomography scans of healthy and glaucomatous eyes. *Biomed Opt Express*. 2013;4:2596-2608.
28. Nadler Z, Wang B, Wollstein G, et al. Repeatability of in vivo 3D lamina cribrosa microarchitecture using adaptive optics spectral domain optical coherence tomography. *Biomed Opt Express*. 2014;5:1114-1123.
29. Hammer DX, Ferguson RD, Mujat M, et al. Multimodal adaptive optics retinal imager: design and performance. *J Opt Soc Am A Opt Image Sci Vis*. 2012;29:2598-2607.
30. Abramoff MD, Magalhães PJ, Ram SJ. Image processing with ImageJ. *Biophotonics Int*. 2004;11:36-43.
31. Doube M, Klosowski MM, Arganda-Carreras I, et al. BoneJ: free and extensible bone image analysis in ImageJ. *Bone*. 2010;47:1076-1079.
32. R Development Core Team. *R: A Language and Environment for Statistical Computing*. Vienna, Austria: R Foundation for Statistical Computing; 2005.
33. Bhandari A, Fontana L, Fitzke FW, Hitchings RA. Quantitative analysis of the lamina cribrosa in vivo using a scanning laser ophthalmoscope. *Curr Eye Res*. 1997;16:1-8.
34. Winkler M, Jester B, Nien-Shy C, et al. High resolution three-dimensional reconstruction of the collagenous matrix of the human optic nerve head. *Brain Res Bull*. 2010;81:339-348.
35. Miller KM, Quigley HA. The clinical appearance of the lamina cribrosa as a function of the extent of glaucomatous optic nerve damage. *Ophthalmology*. 1988;95:135-138.
36. Sigal IA, Flanagan JG, Tertinegg I, Ethier CR. 3D morphometry of the human optic nerve head. *Exp Eye Res*. 2010;90:70-80.